RESEARCH PAPER

Estimation of Wind Load on Stepped Tall Building Using CFD Simulation

Amlan Kumar Bairagi[1] · Sujit Kumar Dalui[1]

Abstract

The behavior of wind around stepped tall building is quite different comparing with the symmetric plan shape tall building. Setback roof of stepped buildings is widely responsible for the turbulence around the building. The purpose of this work is to understand the behavior of wind load on stepped tall building model. Four different models having the same dimensions and same aspect ratios but different setback distances, namely Models A, B, C and D, are considered. The setback distances are $0.2L$, $0.3L$, $0.4L$ and $0.5L$ (L = length) and are located at $H/2$ level (H = height) from the base of domain. Computational fluid dynamics simulations are taken out of terrain category 2 with the model scale 1:300. The foreground of this study is the external pressure and force variation around the building face and roof at 0° and 90° wind incidence angles. Maximum positive pressure coefficient develops at 90% of building height from the base of all models and for setback case it goes to 80%. Negative pressure develops at the building roof top, whereas positive pressure develops in the setback roof for the same model and wind angle. This type of pressure variable will be considered in roof design of stepped building.

Keywords Stepped tall building · Setback roof · Force coefficient · Pressure coefficient · CFD simulation · Wind load

1 Introduction

Numerous high-rise buildings are constructed all over the world. The stepped buildings are widely used in present scenario, and the designers are overwhelming towards versatile configuration changes towards its height. The different types of setback tall buildings were already founded many years ago. The McGraw Hill Building in New York City has setbacks at both sides. The Daily News building, the Western Union building and the Nelson Tower in New York City have multiple setbacks at different levels. The Sears Tower in the USA has a square plan shape with multiple setbacks at different levels. Various wind standards like AS/NZS: 1170.2 (2002), ASCE/SEI 7-10 (2010), BS: 6399-2 (1997), EN: 1991-1-4 (2005) and IS 875: part 3 (2015) discuss some typical plan areas and for unsymmetrical case. Wind tunnel test has been extensively used around the world, and it is valuable too, but computational fluid dynamics (CFD) are much more user-friendly. Kareem (1992) presented the results of a dynamic response of high-rise buildings due to wind and also focused on cross wind and torsional components of aerodynamic loads and their statistical correlations with different aspect ratios. Jain et al. (2001) calculated the effects due to strong wind, mixed strong wind and hurricane wind on a 385 ft tall building using mixed distribution and Monte Carlo simulation. In particular, this study focuses on the effects of coupling, beat phenomenon, amplitude dependence, and structural system type on dynamic properties, as well as correlating observed periods of vibration against finite element predictions. Kijewski-Correa and Pirnia (2007) found and suggested the need for time frequency analyses on dynamic behavior of tall buildings under wind and also highlighted the effect of damping values as well as the comparatively larger degree of energy dissipation. Mendis et al. (2007) enumerated simple quasi-static treatment of wind load on tall buildings. Irwin et al. (2008) established the energy at tall building increased with the increase in the height of tall building. When the width of the building decreased by tapering or setbacks, then the vortices also tried to shade the different frequencies at different heights,

✉ Sujit Kumar Dalui
    sujit_dalui@rediffmail.com

    Amlan Kumar Bairagi
    bairagiak@gmail.com

[1] Department of Civil Engineering, Indian Institute of Engineering Science and Technology, Shibpur, Howrah, India

at the same time fluctuation forces are also reduced. Kim et al. (2008) investigated the effect of tapering on reduced RMS across wind displacement on three aeroelastic, tapered, tall building models with taper ratios of 5%, 10% and 15% and one basic model of a square cross section without a taper were tested using wind tunnel test which simulated the suburban environment. Chan et al. (2009) covered a computer-based technique to minimize the cost of full-scale steel CAARC standard building framework subject to the lateral drift design criteria and an element stiffness optimization due to aerodynamic wind. Amin and Ahuja (2010) presented an overview and modification of the buildings like corner cuts, chamfering of corners, rounding of corners, horizontal and vertical slots, dropping of corners, tapering, etc. Tanaka et al. (2013) studied the aerodynamic response due to wind and flow characteristics of tall buildings with thirty-four numbers unconventional shapes in wind tunnel test and CFD simulation and setback model is one of them. Shiva et al. (2013) highlighted the study and described the value of base shear and twisting moment on five different tall building models with steps near its top and highlight the influence of steps at the top of the building model. Xie et al. (2014) studied aerodynamic optimization of super-tall buildings and its effectiveness assessment on tapering, twisting and stepping and tried to minimize the conflict between optimization scheme and the other design aspects. Mendis et al. (2014) discussed a number of problems, mistakes and solutions for CFD wind analysis. That study also touched on the limitations in wind design code and wind tunnel testing. Baby et al. (2015) presented an overview of optimal external shape and structural system for tall buildings subject to aerodynamic loads and the response of a structure through a comprehensive investigation of the building of different cross sections based on the CFD results. Xu and Xie (2015) focused on the aerodynamic optimization of tall buildings and best compromise wind issues. The authors introduce a method to assess the effectiveness of optimization by tapering, stepping or twisting building elevations that makes use of sectional aerodynamic data derived from a simple wind tunnel pressure testing. Masera et al. (2015) documented two case studies that presented how the wind loads are calculated and applied in design. The first case study is based on the CFD results for the New Marina Casablanca Tower in Casablanca, Morocco. The second case study considers the results from the wind tunnel test studies conducted for the Al-Hamra Tower in Kuwait City. Roy and Bairagi (2016) discussed wind pressure and force coefficients on stepped tall building at different geometrical shapes placed above each other like rectangular, square and triangle. Velocity around the model for different wind angles is also highlighted here. Elshaer et al. (2016) conferred the improvement of the aerodynamic performance of tall buildings by adopted and developed aerodynamic optimization procedure (AOP).

After that, computational fluid dynamics (CFD), optimization algorithm and artificial neural network (ANN) models were used to reliably predict the optimal building shape.

This paper focuses the pressure and force coefficients on different faces and roof for all the models at different setback. The model was analyzed using CFD simulation with wind angle like 0° and 90°. Drastic change of pressure and force was observed at the roof level and also around the building; therefore, special care should be taken to design the setback roof compared to the other roof at the top level. A relation was found between maximum and minimum pressure coefficients at setback roof to help the designer produce a better design.

2 Numerical Study

In computational fluid dynamics (CFD), the $k-\varepsilon$ model is broadly used. The k-ε models use the gradient diffusion hypothesis to relate the Reynolds stresses to the mean velocity gradients and the turbulent viscosity. The turbulent viscosity is modeled as the merchandise of a turbulent velocity and turbulent length scale. k is the turbulence kinetic energy and is defined as the variance of the fluctuations in velocity. It has dimensions of $(L^2 T^2)$; for example, m²/s². ε is the turbulent eddy dissipation and has dimensions of per unit time $(L^2 T^3)$; for example, m²/s³. The $k-\varepsilon$ model introduces two new variables into the system of equations. The continuity equation is such an example:

$$\frac{\partial \rho}{\partial t} + \frac{\partial}{\partial x_j}(\rho U_j) = 0 \tag{1}$$

Moreover, the momentum equation will be

$$\frac{\partial \rho U_i}{\partial t} + \frac{\partial}{\partial x_j}(\rho U_i U_j) = -\frac{\partial p'}{\partial x_i} + \frac{\partial}{\partial x_j}\left[\mu_{eff}\left(\frac{\partial U_i}{\partial x_j} + \frac{\partial U_i}{\partial x_I}\right)\right] + S_M \tag{2}$$

where S_M = sum of body forces; μ_{eff} = effective viscosity accounting for turbulence; p' = modified pressure as defined by:

$$p + \frac{2}{3}\rho k + \frac{2}{3}\mu_{eff}\frac{\partial U_k}{\partial k} \tag{3}$$

The last term in Eq. (3), i.e. $\left(\frac{2}{3}\mu_{eff}\frac{\partial U_k}{\partial k}\right)$ involves the divergence of velocity. It is neglected in CFX. Therefore, this assumption is strictly correct only for incompressible fluids. The $k-\varepsilon$ model is based on the eddy viscosity concept, so that:

$$\mu_{eff} = \mu + \mu_t \tag{4}$$

where μ_t is the turbulent viscosity.

The $k-\varepsilon$ model assumes that the turbulence viscosity is linked to the turbulence kinetic energy and dissipation via the relation:

$$\mu_t = C_\mu \rho \frac{k^2}{\varepsilon} \tag{5}$$

The values of k and ε come directly from the differential transport equations for the turbulence kinetic energy and turbulence dissipation rate:

$$\frac{\partial(\rho k)}{\partial t} + \frac{\partial}{\partial x_j}(\rho k U_j) = \frac{\partial}{\partial x_j}\left[\left(\mu + \frac{\mu_t}{\sigma_k}\right)\frac{\partial k}{\partial x_j}\right] + P_k + P_b - \rho\varepsilon - Y_M + S_k \tag{6}$$

$$\frac{\partial(\rho\varepsilon)}{\partial t} + \frac{\partial}{\partial x_j}(\rho\varepsilon U_j) = \frac{\partial}{\partial x_j}\left[\left(\mu + \frac{\mu_t}{\sigma_\varepsilon}\right)\frac{\partial\varepsilon}{\partial x_j}\right] + \rho C_1 S_\varepsilon - \rho C_2 \frac{\varepsilon^2}{k + \sqrt{\nu\varepsilon}} + C_{1\varepsilon}\frac{\varepsilon}{k}C_{3\varepsilon}P_b + S_\varepsilon \tag{7}$$

where

$C_1 = \max\left[0.43, \frac{\eta}{\eta+5}\right], \eta = S\frac{k}{\varepsilon}, S = \sqrt{2S_{ij}S_{ij}}.$

Here P_k = the generation of turbulence kinetic energy due to the mean velocity gradients; P_b = the generation of turbulence kinetic energy due to buoyancy; Y_M = the contribution of the fluctuating dilatation in compressible turbulence to the overall dissipation rate. Where $k-\varepsilon$ turbulence model constant $C_{1\varepsilon}$ = 1.44, $k-\varepsilon$ turbulence model constant C_2 = 1.92, turbulence model constant for the k equation σ_k = 1.0 and $k-\varepsilon$ turbulence model constant σ_ε = 1.2.

2.1 Building Model

Square plane shape tall building is characterized as a bluff body with setback roof at $H/2$ from base used in this study using CFD simulation. Four numbers of setback building models are used in this study. The models are square plan shape of Length (L) = 250 mm, Breadth (B) = 250 mm and Height (H) = 500 mm of scale 1:300 with terrain category 2. Many researchers like Zils and Viise (2003) suggested that the wind tunnel models scale varied between 1:100 and 1:600 for high-rise buildings and were placed on the turntable for considering them as appropriate loading for overall lateral system design; and cladding design predicts motion perception and pedestrian level effects. Yan and Li (2015) simulated the square prism 1:250 scale with blockage ratio 3%. Zu and Lam (2018) studied the highest scale 1:1000 model scale for full-scale building model height 180 m and width 30 m. Azziz et al. (2020) guided the 1:20 to 1:50 length scale range for low-rise buildings. Presently, the length scale (1:300) was adopted for the study. If the model was to be full scale, then the analytical process would be quite complicated and to avoid high computational facilities, excessive run time as the number of elements is very high. The properties are the same for all four models, therefore the

aspect ratios are also the same, but the setback distances are different. Considered setback distance for Model A is $0.2L$ from Face D1. Similarly, the setback distance for models, namely Models B, C and D, is $0.3L$, $0.4L$ and $0.5L$ from Face D1, respectively. This setback distance set up at H/2 height from base of the models. A good number of researchers Kim and Kanda (2010, 2013), Kim et al. (2011), Mittal et al. (2018) Bairagi and Dalui (2019), Rej and Bairagi (2019) already studied the variation of different aerodynamic parameters of setback building models and most of the building models have setback at half height of the building with constant setback distance. Kim and Kanda (2013) suggested that the setback buildings experienced an extensive amount of wind pressure and turbulence near the setback region. According to this consideration, this study focuses on the different wind parameters of setback buildings with a variable setback at half of the building height. This study is based on wind incidence angels 0° and 90°. Wind projected on building parallel to Y-axis is 0° and parallel to X-axis is 90°. Face name of all four models is Face A, Face B, Face C, Face D1, Face D2, Roof R1 and Roof R2 as shown in Fig. 1. Bairagi and Dalui (2018) studied wind pressure around different types of single and double setback tall buildings. Due to the limitation of the page, the number of selected building models is pretty much limited to only one general configuration. The number and position of setbacks, i.e., only one setback at building mid-height which is placed at four different setback distances.

2.2 Boundary Condition

The numerical study carried out by CFD simulation adopted the same boundary condition. The inlet, lateral and top boundary were considered $5H$ (H = building height) from the model, and outflow boundary should be placed at $15H$ behind the model to allow for proper flow development as recommended by Frank et al. (2004), Revuz et al. (2012). The direction constraint requires that the flow direction be parallel to the normal boundary surface that is calculated at each element face on the inlet boundary. For no slip wall (not moving, no wall velocity), the velocity of the fluid at the wall boundary is set to zero, so the boundary condition for the velocity becomes U_{wall} = 0. For free slip wall the velocity component parallel to the wall has a finite value, but the velocity normal to the wall, and the wall shear stress, are both set to zero: U_{wall} = 0, τ_w = 0. The velocity profile of the atmospheric boundary layer in the CFD was calculated by the following power law:

Fig. 1 Building models used
in CFD analysis **a** Model A, **b**
Model B, **c** Model C and Model
D

Model A
(a)

Model B
(b)

Model C
(c)

Model D
(d)
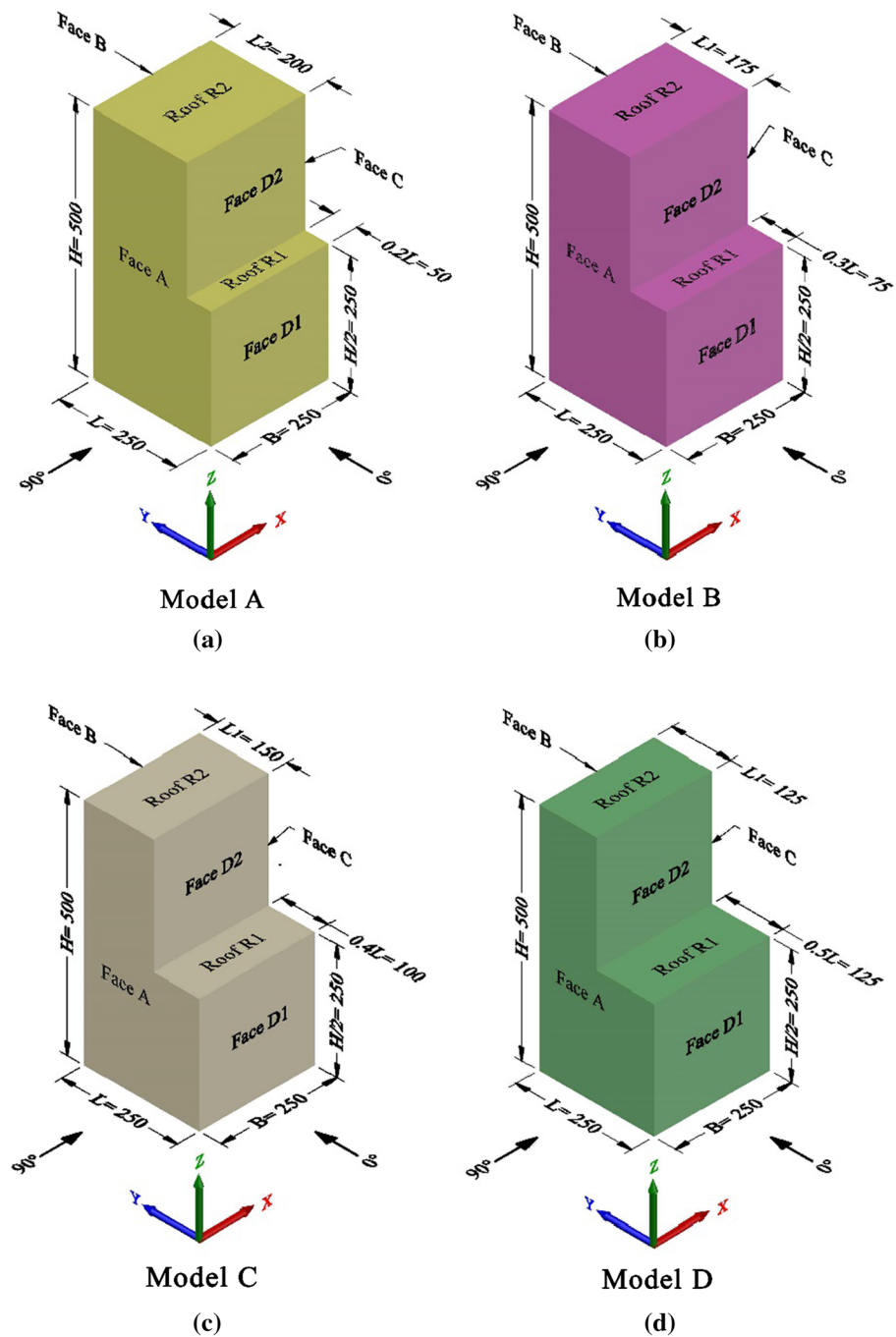
$$\frac{U}{U_h} = \left(\frac{Z}{Z_h}\right)^{\alpha} \tag{8}$$

where U is the horizontal wind speed at an elevation Z; U_h is the speed at the reference elevation Z_h; which was 10 m/s; α is the parameter that varies with ground roughness that is 0.133 for terrain category 2. Z_h is 1.0 m in this case. The kinetic energy of turbulence and its dissipation rate at the inlet section were calculated according to the following equations:

$$k = \frac{3}{2}\left(U_{avg}I\right)^2 \text{ and } \varepsilon = C_\mu^{\frac{3}{4}}\left(\frac{k^{\frac{3}{2}}}{l}\right) \tag{9}$$

where U_{avg} is the mean velocity at inlet; I is the turbulence intensity; l is the turbulence integral length scale. Normal air temperature 25 ℃ is considered in the domain and $k-\varepsilon$ turbulence model. Building walls are no slip condition, but sidewall, building top and top of domain are free slip condition. The figure of domain referred by Bairagi and Dalui (2018) is shown in Fig. 2.

2.3 Meshing of Computational Model

Mesh adaption in CFX is the process in which, once or more during a run, the mesh is selectively refined in areas that depend on the adaption criteria specified. This means that as the solution is calculated, the mesh can automatically be refined in the most significant condition. The tetrahedron meshing is used and inflated near the boundary. This meshing is used for all models in CFD simulation to avoid the unusual flows. Fine meshing is used for the models for better results. The similar type of course, fine discretized mesh and meshing of square plan shape and $0.2L$ setback building model suggested by Bairagi and Dalui (2018) are shown in Figs. 3 and 4, respectively.

2.4 Square Plan Shape Tall Building

2.4.1 Pressure Distribution on Square Plan Shape Tall Building

A square plan shape with uniform cross-sectional tall building having the same plan area (62,500 mm^2) in comparison with stepped model is considered to validate this study in using CFD simulation. The isolated square plan shape with uniform cross-sectional tall building has $L = 250$ mm, $B = 250$ mm, $H = 500$ mm. This building can abide 0° wind at Face A which is parallel to X-axis and 90° wind angle at Face D which is parallel to Y-axis as shown in Fig. 5a. As the symmetry in the plan is about X and Y axis, so the nature of C_{pe} at Face A due to 0° wind should be the same for 90° wind at Face D. When the building could withstand 0° wind angle, Face A and Face C responded as windward and leeward face with positive and negative pressure, respectively. At the same time, Faces B and D experienced suction. Velocity profile has been drawn at the inlet position of the square plan shape building and this profile is the same as stated in S.P 64 (S&T): (2001) see Fig. 5b. Kwon and Kareem (2013) also focused the comparative study of major international wind codes and standards for wind effects on tall buildings. Weerasuriya and Jayasinghe (2014) evaluated the wind load on high-rise building using five major international wind codes in both ultimate and serviceability limit conditions. Bairagi and Dalui (2018) compared the CFD results of pressure and force coefficients of the same type of 1:1:2 (length:breadth:height) square bluff body with the AS/NZS: 1170.2 (2002), ASCE/SEI 7-10 (2010), EN: 1991-1-4 (2005), BS: 6399-2 (1997) and IS 875: part 3 (1987) as shown in Tables. 1 and 2. The similar typeface name, contour diagrams and streamline of square plan shape model for 0° wind angle studied by Bairagi and Dalui (2018) are shown in Fig. 6.

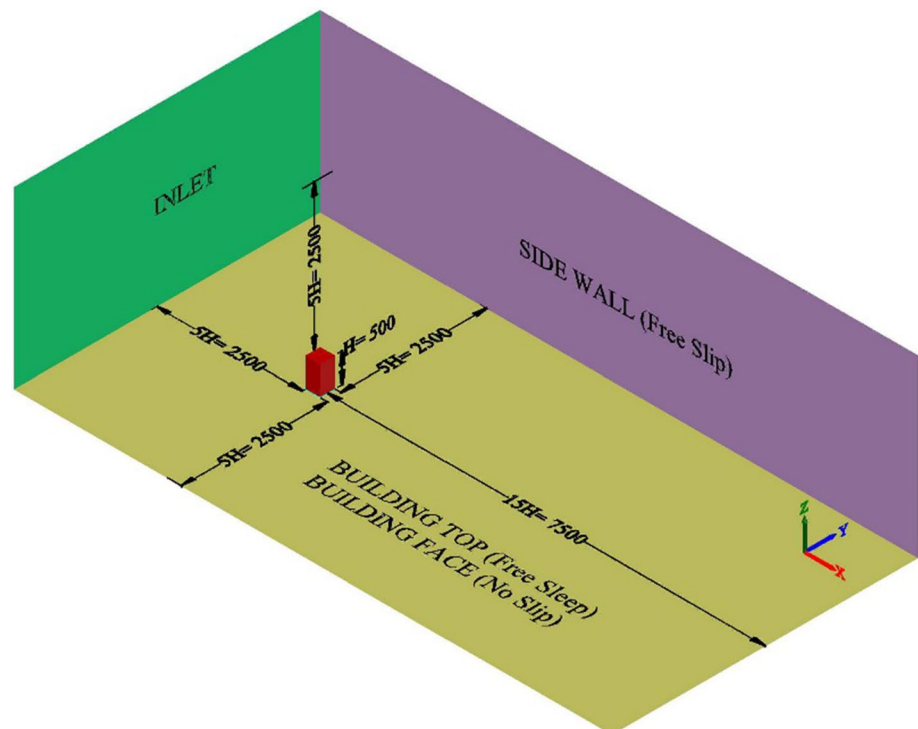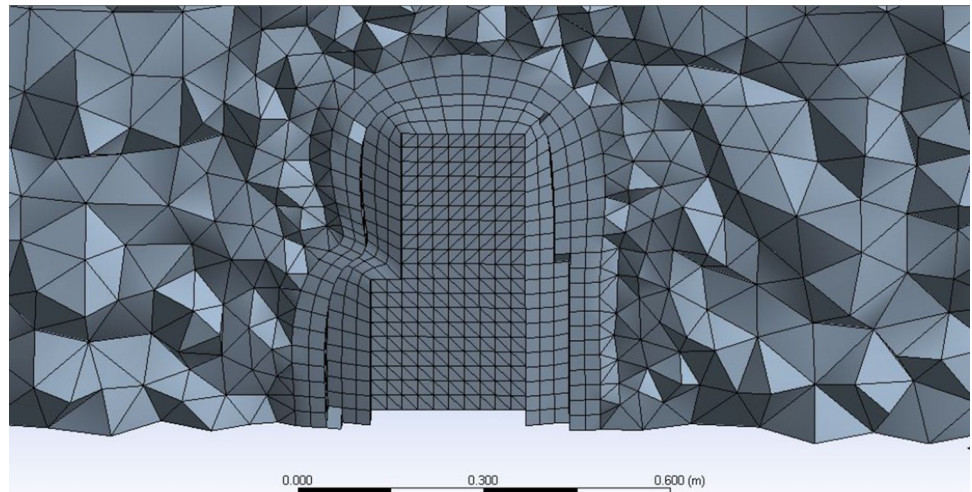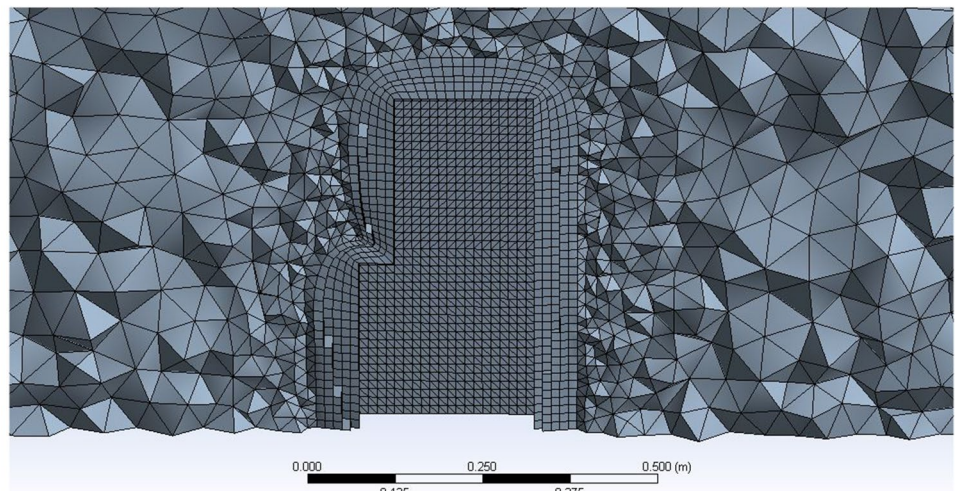**Fig. 2** Computational domain and boundary conditions

Fig. 3 Meshing variation on stepped tall building using different discretization **a** Course discretized meshing, **b** fine discretized meshing
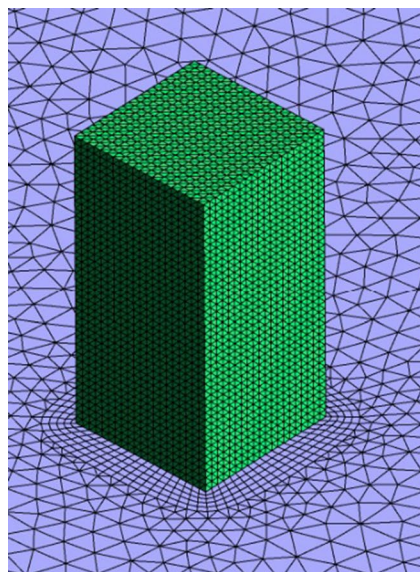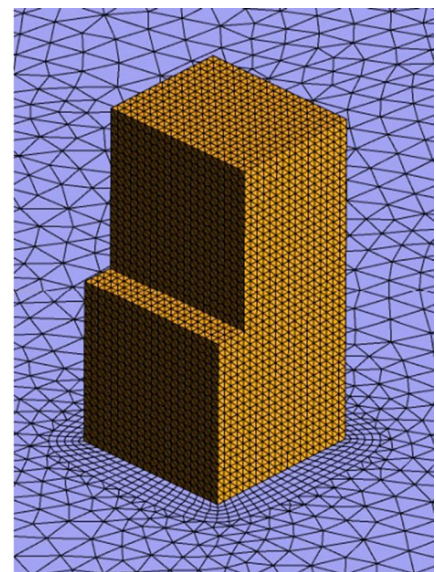
(a)

(b)

Fig. 4 Meshing of different buildings and domain **a** square plan shape tall building, **b** stepped model with 0.2L setback distance

(a)   (b)

Fig. 5 a Square plan shape with uniform cross-sectional tall building showing dimension and face details, **b** velocity profile of square plan shape model for 0° wind angle
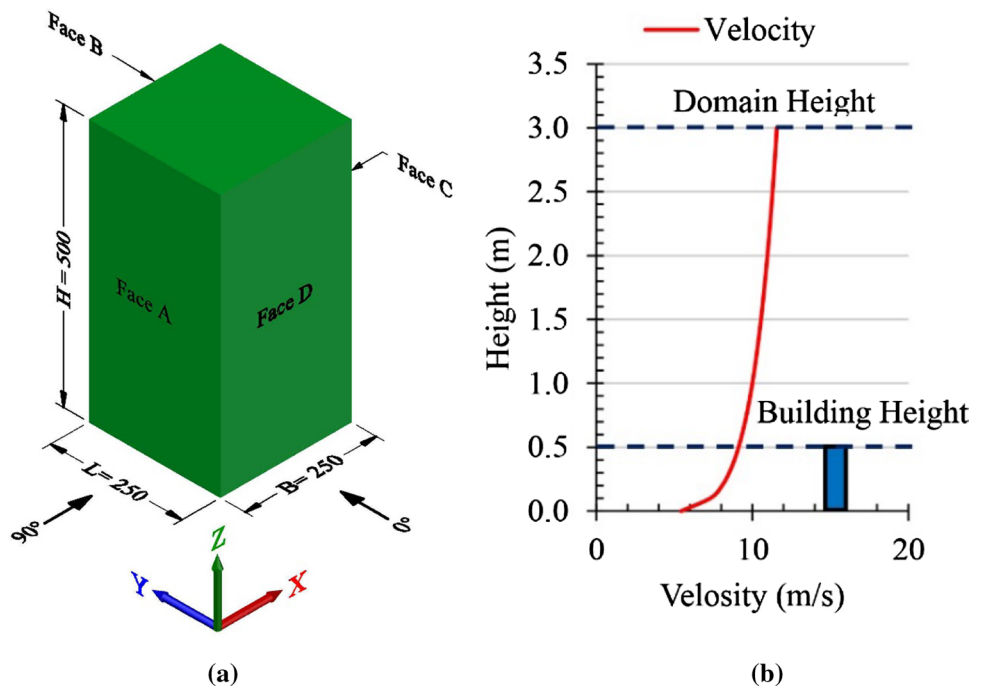

(a)   (b)

Table 1 Comparison of surface pressure coefficient (C_{pe}) on square plan shape tall building

Location	Pressure coefficient as per											
	ANSYS CFD		AS/NZS: 1170.2: 2002		ASCE/SEI 7-10: 2010		EN 1991-1-4:2005		BS 6399-2: 1997		IS:875 (Part 3)-2015	
	0°	90°	0°	90°	0°	90°	0°	90°	0°	90°	0°	90°
Windward side	0.8	0.8	0.8	0.8	0.8	0.8	0.8	0.8	0.76	0.76	0.8	0.8
Leeward side	−0.5	−0.5	−0.5	−0.5	−0.5	−0.5	−0.55	−0.55	−0.5	−0.5	−0.25	−0.25
Sidewalls	−0.7	−0.7	−0.65	−0.65	−0.7	−0.7	−0.8	−0.8	−0.8	−0.8	−0.8	−0.8

Table 2 Comparison force coefficient on vertical surface of square plan shape tall building

| Force coefficient (Cf) as per				
ANSYS CFD	AS/NZS: 1170.2: 2002	ASCE/SEI 7–10: 2010	EN 1991–1-4:2005	IS:875 (Part 3)-12,015
1.28	2.2	1.31	2.1	1.20

2.5 Analytical Results

CFD simulation has been done for Models A, B, C and D at 0° and 90° wind angle. Facewise comparative study of different models was also carried out in this field.

### 2.5.1 Vertical Pressure Coefficient for Models A, B, C and D Due to Wind Angle 0° and 90°

External pressure coefficients (C_{pe}) at different faces of all the models have been observed for 0° and 90° wind angles.

A vertical line was drawn at the Face A and Face C at a distance of $L_1/2$ to calculate C_{pe}. Furthermore, a vertical line was drawn at Faces B, D1 and D2 at B/2 distance. The associated figures are depicted in Table 3 under column named building model. Graphical representation of facewise vertical C_{pe} for different models for 0° and 90° wind angles are also presented in this table. The C_{pe} values for Models A, B, C and D are negative for Face A and Face C for 0° wind angle. Here C_{pe} values of Models B, C and D coexist with each other, in spite of Model A presenting a different suction pressure due to its setback distance 0.2L. The positive C_{pe} values for all four models converge to each other at Face A due to 90° wind angle. In this case, the maximum positive pressure coefficient (1.19) originated at 440 mm height that is 0.9H from the base of the model. C_{pe} value for all models at Face B for 0° and 90° wind angle presented negative pressure when the face is leeward for 0° and sidewall for 90° wind. When wind-attacking angle is 90°, the Face B reacts as sidewall face. For 90° wind angle, Face C reacts with suction to be a leeward face. C_{pe} values for all the models below

Fig. 6 Face name, contour and streamline of square plan shape tall building for 0° wind angle
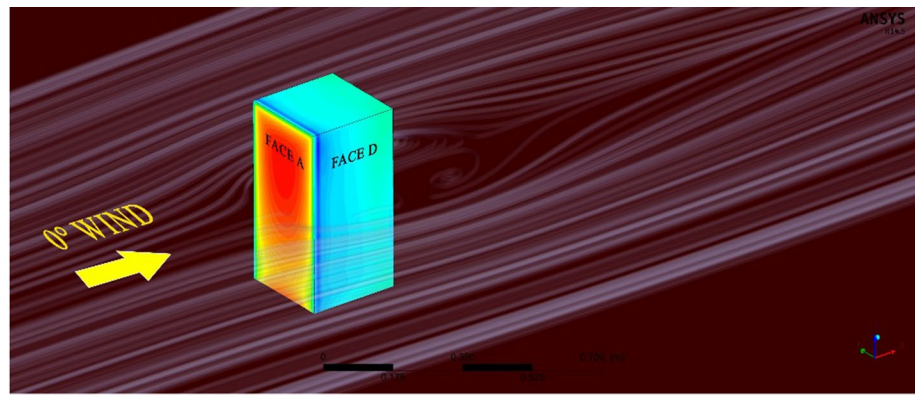
(a)
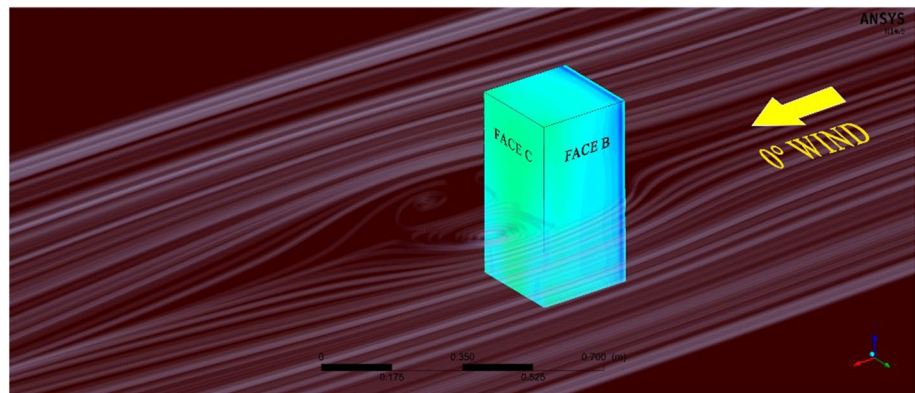
(b)

$H/2$ height gradually fall down from Model A to Model D. Faces D1 and D2 have an offset distance of 0.2L for Model A, 0.3L for Model B, 0.4L for Model C and 0.5L for Model D. The Faces D1 and D2 responded as windward face due to 0° wind, so the C_{pe} values are positive for all the models, and maximum positive pressure (1.13) is located at height 390 mm that is 0.8H from the base of the model. Here, a crucial point is observed at $H/2$ level. At $H/2$ level, a kink portion developed by C_{pe} due to the offsets of building. For 90° wind angle, Faces D1 and D2 are the side face. It is fair that the C_{pe} values for Model A and Model B are playing along each other, in addition the C_{pe} for Models C and D are going in the same way. In addition, the pressure difference develops at the kink portion at $H/2$ level of the models due to its offset. Table 3 Vertical C_{pe} due to 0° and 90° wind angle at different faces for Model A, Model B, Model C and Model D.

2.5.2 Horizontal Pressure Coefficient for Models A, B, C and D Due to Wind Angle 0° and 90°

C_{pe} around the models at different elevation due to 0° and 90° wind are also discussed here. Horizontal line was drawn around the outskirts of the building at $H/4$, $12H/25$, $13H/25$

and $3H/4$ level from base of the building. A general building model where lines are 1–2–3–4–1 at H/4 level, 1′–2′–3′–4′–1′ at 12H/25 level, 5′–6′–7′–8′–5′ at 13H/25 and 5–6–7–8–5 at 3H/4 level is shown in Fig. 7. For 0° wind angle, pressure line 1′–2′ and 3′–4′ is sidewall of all the models, again 2′–3′ and 4′–1′ is windward and leeward face, respectively. From Fig. 8 a, maximum suction (− 1.109) developed in Model D at 3′–4′ belt and minimum suction (− 0.327) at 4′–1′ region in Model A. Though boundary of Models A, B, C and D is the same at zone 1′–2′–3′–4′–1′, maximum suction at face A switched moderately from 222 to 167 mm according to the change of model setback distance. Maximum positive C_{pe} (1.082) was established due to minimum setback, i.e., 0.2L distance and sank steadily due to inflation of setback distance. Suction on the leeward side at sector 4′–1′ has been also decreased from Model A to Model D. Here maximum suction pressure evolved on Model D due to its maximum setback length.

Horizontal external pressure coefficient at level $13H/25$, namely 5′–6′–7′–8′–5′ carrying different perimeter length due to its various setback distance as shown in Fig. 8b, so the graph length at this level is changing according to the perimeter. Moreover, the length of line 5′–6′ and 7′–8′ is varying with different setback distances. Length of these

Table 3 Vertical C_{pe} due to 0° and 90° wind angle at different faces for Model A, Model B, Model C and Model D

Vertical C_{pe} for 0° wind angle	Building Model	Vertical C_{pe} for 90° wind angle

two lines is 200 mm for Model A, 175 mm for Model B, 150 mm for Model C and 125 mm for Model D. Lines 6′–7′ and 8′–5′ have constant length of 250 mm. Maximum negative pressure (− 0.901) developed for Model D in side face of the building, i.e., 7′–8′ zone and minimum negative pressure (− 0.307) for Model A at leeward face, i.e., 8′–5′ belt for 0° wind angle. A remarkable positive pressure difference was observed due to setback distances at 6′–7′ zone. Where maximum C_{pe} (1.118) developed at windward face for Model D at 6′–7′ region. Figures 9, 10 and 11 present the graphical representation of horizontal

C_{pe} for 90° wind angle around the perimeter of the building at 12H/25 and 13H/25 level. Maximum C_{pe} (1.096) value grows up at 1′–2′, i.e., 12H/25 belt in Model A. An impressive change of pressure has been developed at this height. The C_{pe} for all the models is suddenly sunk after 111 mm (0.444L) distance from point 1′ and concluded after 222 mm (0.888L) distance from 1′. High suction pressure (− 1.481) developed at zone 2′–3′ for Models A and B, in spite of Models C and D that presented minimum C_{pe} (− 0.245). Again another side face D1 at 4′–1′ zone, the C_{pe} for Models A and B chased each other, escalating

Fig. 7 Typical diagram of different level of horizontal pressure coefficient around the building Model A. Similar type of pressure levels considered for Models B, C and D
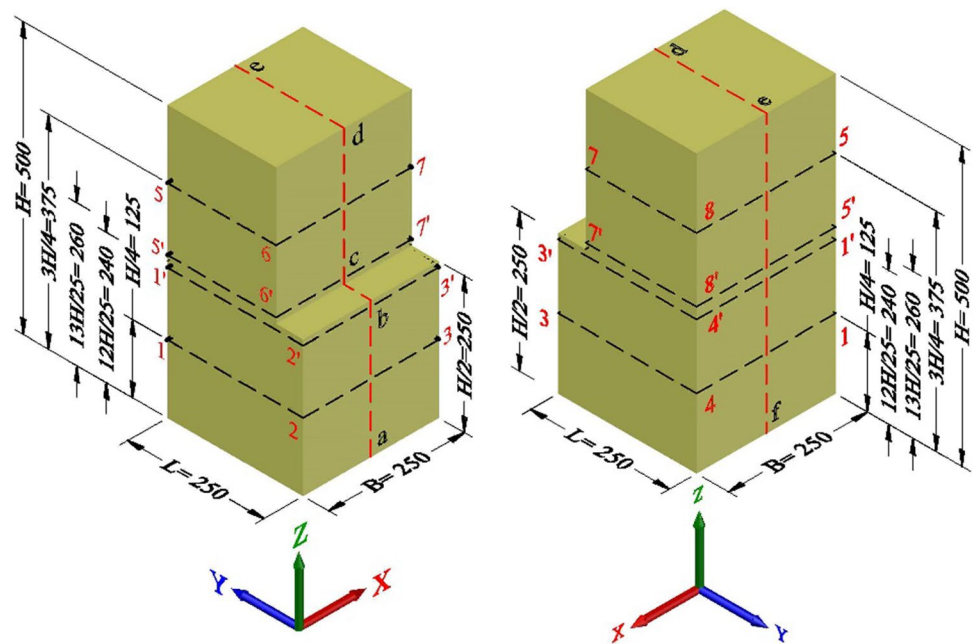
the suction. Additionally, Models C and D drive negative pressure towards heavy suction region.

The pressure difference at belt 1′–2′, the summit point, i.e., 0.444L and the valley point, i.e., 0.888L are represented in percentage under Table 4. Here, the difference of maximum fall of pressure in percentage has been shown under Model C, which is 47.22% and minimum for the Model B, i.e., 23.75%. The change of pressure contour at Face A for Models A, B, C and D at 1′–2′ level for 90° wind angle is shown under Fig. 10.

Figure 11 represents another pressure zone at level 13H/25, i.e., 5′–6′–7′–8′–5′ to calculate pressure coefficients. C_{pe} at this level have also had the same behavior as in level 12H/25. Maximum positive C_{pe} (1.129) develop at windward face for 90° wind angle at 5′–6′ zone, whereas suction pressure develops at 6′–7′–8′–5′ zone of all the models. Minimum pressure fluctuation is observed in 6′–7′ region because of the 0.2L–0.3L and 0.4L–0.5L setback distance. Spectacular pressure variation located between 0.3L and 0.4L offset at 6′–7′ region. Maximum suction pressure (− 1.527) is recorded at leeward face on Model B and minimum suction pressure (− 0.242) at sidewall for Model C.

Detailed estimates of maximum and minimum C_{pe} at 12H/25 and 13H/25 level for Models A, B, C and D at 0° and 90° wind angle are discussed under Table 5. The magnitude of external pressure coefficients for Models A, B, C and D at H/4 and 3H/4 level due to 0° and 90° wind angles is shown in Table 6. Magnitude of pressure variation comparing with different models according to 0° wind angle is shown in Table 7.

2.5.3 Comparison of Pressure Coefficient at Roof R1 and R2 for 0° wind Angle for Models A, B, C and D

Variation of external pressure coefficients at Faces D1, D2, B and Roof R1, R2 for Models A, B, C, D at 0° wind angle was also carried out in this study. For this particular angle, Faces D1 and D2 are windward face and Face B is leeward face. A line a–b–c–d–e–f has been drawn in vertical periphery and was placed at the center position of Face D1, i.e., B/2 = 125 mm from base to the top of the building height as shown in Fig. 7. Line a–b and c–d is 250 mm and line c–d and d–e has variable length for model to model. For Model A, the length of b–c is 0.2L, i.e., 50 mm. For Model B, it is 0.3L, i.e., 75 mm. For Models C and D, it is 0.4L and 0.5L, i.e., 100 mm and 125 mm, respectively. Similarly, the length d–e for Models A, B, C and D is 200 mm, 175 mm, 150 mm and 125 mm. Therefore, the curve length at this kink portion is varying with the offset length as shown in Fig. 12. It is important to note that here, the pressure at Roof R1, i.e., b–c zone for Model A has a maximum positive value comparing to the other models. The value of Model D at this region progressed towards the negative direction (− 0.045). Another curious criterion has been highlighted in this graph. The minimum positive pressure positioned in roof at 11 mm from point 'b', which is 261 mm from point 'a', is also for the Model A. Therefore, it can be stated that the minimum positive pressure at roof for 0.2L setback distance is located at 0.044L from the edge of kink, i.e., 4.4% of length of the building. On the other hand, Roof R2 experienced negative pressure for all the models. The negative C_{pe} at d–e

Fig. 8 Horizontal external pressure coefficient for Models A, B, C and D at 0° wind angle **a** at 12*H*/25 level, **b** at 13*H*/25 level

HEIGHT 12H/25

(a)

HEIGHT 13H/25

(b)
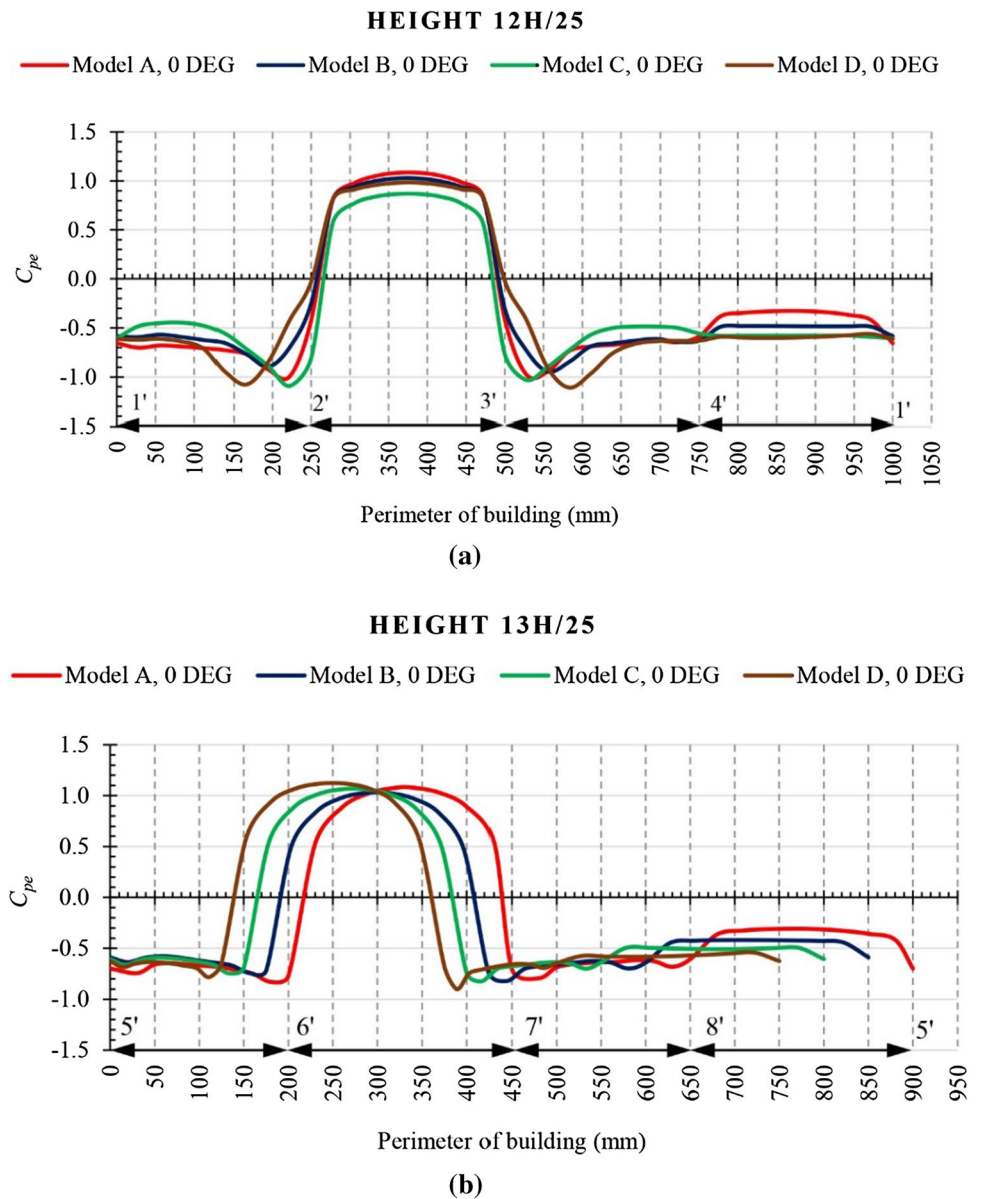
location also changed according to the setback distances of different models as shown under Fig. 12 in *d–e* region. The position of maximum and minimum C_{pe} has also been calculated from the edges of both R1 and R2 roofs, i.e., from point '*b*' and '*d*', respectively. The maximum and minimum negative C_{pe} values at roof R1 and R2 developed at 20% and 4.4% of length of the building for Model A. Similarly, the location of maximum and minimum C_{pe} at roof R1 and R2 for all the models is calculated and shown in Table 8. From this table it is fair that the maximum positive C_{pe} developed at the extreme setback distance on R1 and maximum negative C_{pe} matured at the starting edge of the R2 for all the models. Figure 13 shows the graphical representation of location of maximum and minimum C_{pe} from edge of the setback roofs for different models in

percentage with the length of the building. After plotting the values from Table 8, a linear line has been progressed for maximum and minimum pressure coefficients in order to gradually change setback distances. Using this figure, the designers will calculate the location of maximum and minimum C_{pe} from the edge of setback roof of different models. As an example, considering offsetting distance for a model is 0.35*L*, which is in between two offset distances, 0.3*L* and 0.4*L*. Therefore, the location of maximum C_{pe} for setback roof is 35% of length of the building. Similarly, the location of minimum C_{pe} was observed at 14% of the length of the building. Again, the maximum C_{pe} is located at 15% length and minimum C_{pe} at the location is 22% of the length of the building.

Springer

Fig. 9 Horizontal external pressure coefficient at 12*H*/25 level for Models A, B, C and D at 90° wind angle
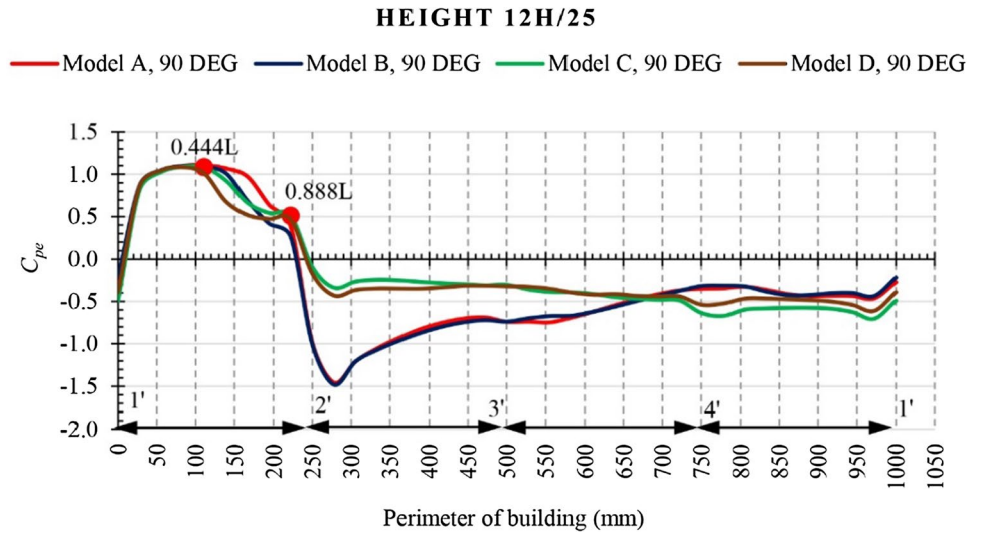

Fig. 10 Pressure contour for comparison of horizontal C_{pe} at 12*H*/25 level for 1′–2′ zone **a** Model A, **b** Model B, **c** Model C, **d** Model D
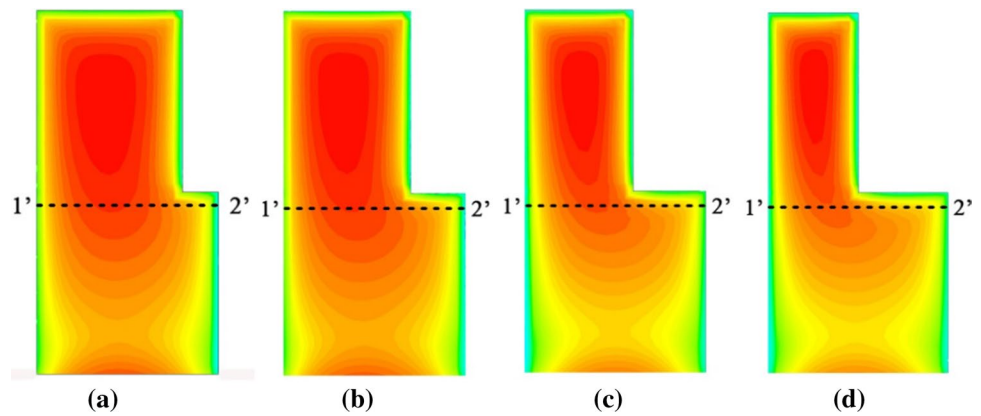

Fig. 11 Horizontal external pressure coefficient at 13*H*/25 level for Models A, B, C and D at 90° wind angle
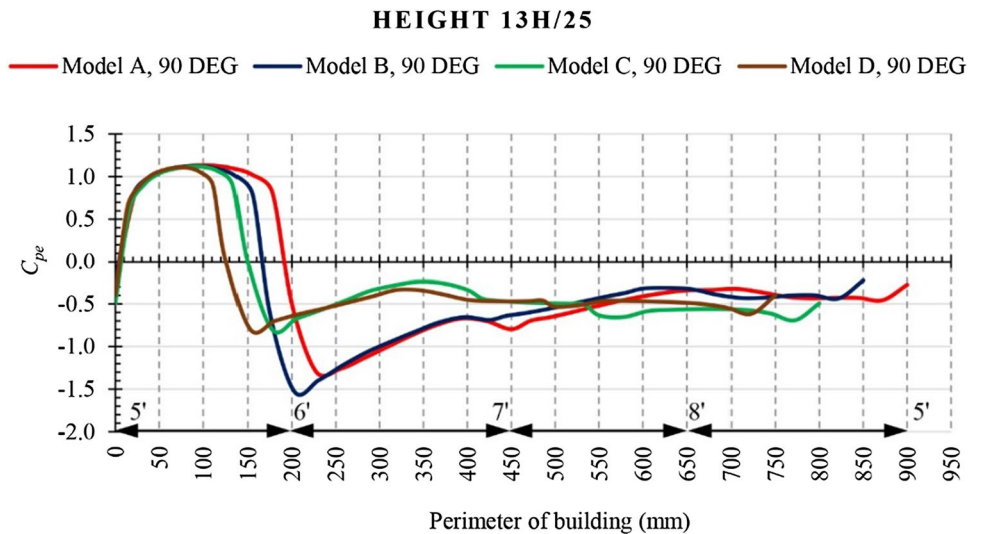
Table 4 Percentage fall of C_{pe} from 2′ to 1′ for Models A, B, C and D

Model no.	Location of positive C_{pe} at 1′–2′		Percentage fall between 0.444L and 0.888L (%)
	0.444L	0.888L	
A	1.106	0.379	34.26
B	1.086	0.258	23.75
C	1.082	0.511	47.22
D	1.011	0.466	46.09

2.5.4 Pressure Contour of Different Faces and Roofs of Models A, B, C and D at 0° wind Angle

Pressure contour for different faces like A, B, C, D1, D2 and roof of the models R1 and R2 for 0° wind incidence angle are explained in Table 9. Close up view of streamline at the setback region of all the models is shown in Table 10. The pressure at Roof R1 is positive for all the models, and the pressure gradually decreases with the increase in setback distance. Again, for Roof R2, the pressure is suction for all the models. Local pressure developed only at the lower sidewalls of all the building models, i.e., lower step of Faces A and D for 0° wind angle. However, no local pressure developed due to the setback distance at the upper inset sidewalls. The detailed explanation has already been discussed in previous articles. Thus, extra care should be considered to design the setback roof.

2.5.5 Fluctuation of Wind Velocity

Non-dimensional streamwise velocity profile has already been studied by several researchers. The 1:1:2 (length: breadth: height) square plan shape building model was studied by Meng and Hibi (1998), Tominga et al. (2008), Wang et al. (2015) and Gosseau et al. (2013). According to this consideration, this study adopted the model of the same aspect ratio. The past researchers considered the non-dimensional profile locations at $x/b = -0.75$; -0.25; 0.5; 1.25 and 3.25 and plotted the mean streamwise velocity profile to observed the velocity variation. However, in this study, the along wind velocity was considered at Y-axis; therefore the non-dimensional velocity profile location was designated by x/b. For the across wind condition, the profile locations are fixed at y/b. The non-dimensional height of the wind profile is represented as z/b, where the x, y and z are the coordinates of the building model inside the domain and b is represented as the breadth of the building model. In this study, the analytical model was placed inside the domain (Frank et al. 2007; Tominaga et al. 2008a, b) and was applied along the wind flow on Y-axis. Therefore, the mean streamwise velocity profile was drawn at $y/b = -0.75$; -0.25; 0.5; 1.25 and 3.25 as shown in Fig. 14a. Similarly, the across wind flow was adopted on X-axis. Therefore, the mean streamwise velocity profile was plotted at locations $x/b = -0.75$; -0.25; 0.5; 1.25 and 3.25 as shown in Fig. 14b. Figure 14a represents the high-velocity fluctuation at -0.25 profile, which is located at the setback region of the Models A, B, C and D. The non-dimensional velocity (U/U_h) of Model A was observed 0.21 at the top of setback ($z/b = 1.0$). At this particular location ($z/b = 1.03$) the U/U_h gradually increased from 0.24, 0.44 and 0.72 for the Models B, C and D, respectively. This high amount of fluctuating velocity was not observed in other profiles. The velocity profile was located at $x/b = -0.25$ for across wind condition, the Model D deserved $U/U_h = 0.30$ at $z/b = 1.0$ level as shown in Fig. 14b. No response of velocity variation was observed at $z/b = 1.0$ level for Models A, B and C due to its different setback length. An important point was found at $x/b = 1.25$ profile. The tremendous velocity variation was observed $z/b = 1.07$ and 2.04 level. Finally, two important points emerge. First, the velocity at the setback level increases with

Table 5 Comparison of maximum and minimum C_{pe} for models A, B, C, D

C_{pe} at level	Wind angle	Type of pressure	C_{pe} value	Building side	Level marked	Model name	Setback distance
12H/25	0°	Maximum (−)	−1.109	Side face	3′–4′	D	0.5 L
		Minimum (−)	−0.327	Leeward	4′–1′	A	0.2 L
		Maximum (+)	1.082	Windward	2′–3′	A	0.2 L
	90°	Maximum (−)	−1.481	Windward	2′–3′	B	0.3 L
		Minimum (−)	−0.245	Side face	4′–1′	D	0.5 L
		Maximum (+)	1.096	Side face	1′–2′	B	0.3 L
13H/25	0°	Maximum (−)	−0.901	Side face	7′–8′	D	0.5 L
		Minimum (−)	−0.307	Leeward	8′–5′	A	0.2 L
		Maximum (+)	1.118	Windward	6′–7′	D	0.5 L
	90°	Maximum (−)	−1.527	Leeward	6′–7′	B	0.3 L
		Minimum (−)	−0.242	Side face	6′–7′	C	0.4 L
		Maximum (+)	1.129	Windward	5′–6′	A	0.2 L

Table 6 Wind pressure diagram at level $H/4$ and $3H/4$ for models A, B, C and D for 0° and 90° wind angle

Model	Pressure at level	Pressure diagram	
		0° Wind	90° Wind
Model A	$H/4$		
	$3H/4$		
Model B	$H/4$		
	$3H/4$		
Model C	$H/4$		
	$3H/4$		
Model D	$H/4$		

Table 6 (continued)

Model	Pressure at level	Pressure diagram	
		0° Wind	90° Wind
	3*H*/4		

Table 7 Variation of magnitude of mean surface pressure coefficient on different faces of Models A. B, C and D due to change in wind incidence angle

Model name	Location	Avg (C_{pe}) for 0° angle	Avg (C_{pe}) for 90° angle	Change in magnitude (w.r.t 0°)		Remarks
				Increase in %	Decrease in %	
Model A	Face A	−0.66	0.67	1.5*		*Indicates change in nature of wind pressure
	Face B	−0.42	−0.43	2.4		
	Face C	−0.65	−0.52		20	
	Face D1	0.62	−0.95	53.2*		
	Face D2	0.74	−0.84	13.5*		
	Roof R1	0.69	−0.91	32*		
	Roof R2	−0.66	−0.57		13.6	
Model B	Face A	−0.63	0.63	0*		
	Face B	−0.46	−0.42		8.7	
	Face C	−0.67	−0.51		24	
	Face D1	0.60	−0.94	56.7*		
	Face D2	0.72	−0.93	29.2*		
	Roof R1	0.58	−0.97	67.2*		
	Roof R2	−0.61	−0.64	4.8		
Model C	Face A	−0.63	0.66	4.8*		
	Face B	−0.48	−0.60	25		
	Face C	−0.66	−0.35		47	
	Face D1	0.61	−0.34		44.3*	
	Face D2	0.73	0.54		26*	
	Roof R1	0.46	−0.43		6.5*	
	Roof R2	−0.67	−0.51		24	
Model D	Face A	−0.65	0.64		1.5*	
	Face B	−0.51	−0.52	2		
	Face C	−0.67	−0.30		55.2	
	Face D1	0.61	−0.39		36.1*	
	Face D2	0.74	−0.58		21.6*	
	Roof R1	−0.38	−0.58	52.6		
	Roof R2	−0.64	−0.54		15.6	

Fig. 12 Comparison of C_{pe} at line a–b–c–d–e–f for Models A, B, C and D at 0° wind angle
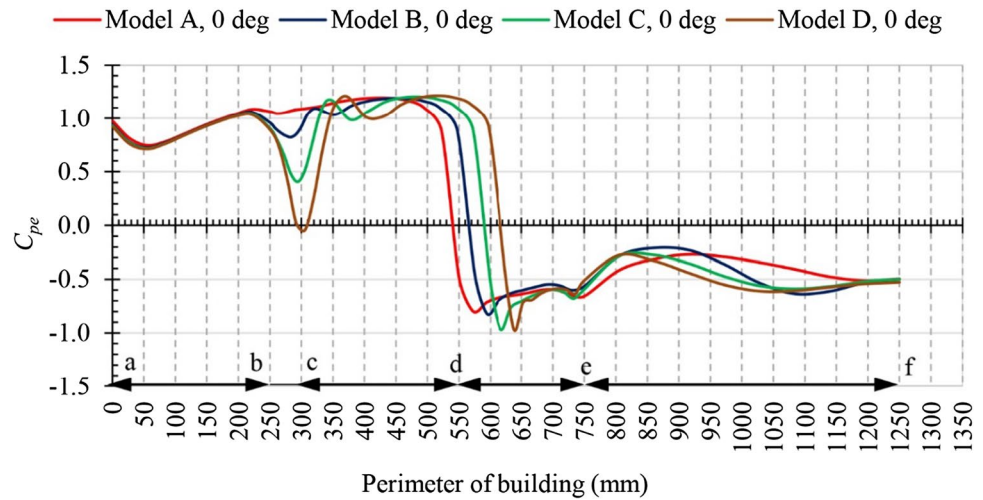

Table 8 Minimum and maximum C_{pe} at Roof R1 and R2 for different Models A, B, C and D for 0° wind angle

Model name		Model A	Model B	Model C	Model D
Setback distance		0.2L (%)	0.3L (%)	0.4L (%)	0.5L (%)
Roof R1, line b–c	C_{pe} max located from 'b' in % of length	20	30	40	50
	C_{pe} min located from 'b' in % of length	4.4	13.2	17.6	22.4
Roof R2, line d–e	C_{pe} max located from 'd' in % of length	2	10	20	30
	C_{pe} min located from 'd' in % of length	9	18	27	36

the increase in setback distance. It means that the velocity is directly proportional to setback distance at that particular setback model. Secondly, a high amount of turbulence and velocity fluctuation is observed near the setback roof and top roof region at the backside of the building model.

2.5.6 Force Coefficient (C_f) for Models A, B, C, D at 0° and 90° wind angle

When a force is acting on a body opposite the relative motion, which is moving with respect to the surrounding fluid, it can exist between the fluid and the solid surface. In this case, the fluid is wind and the solid surface is building model. Again, drag force depends upon the velocity. All the same, in this experiment, velocity of wind is the same for all the iterations, but the change of exposure area due to different setback the drag force is also varied. Once more, this exposure area changes with the change of wind incidence angle. Consequently, drag forces are different as well as force coefficients are changed with wind angles. Simiu and Scanlan (1996) discussed the drag coefficient equation:

$$F_D(t) = \frac{1}{2}\rho v^2(t)B^2 C_d \qquad (10)$$

where $F_D(t) =$ the time varying drag on a body, $\rho =$ density of the fluid, $v(t) =$ speed of the object relative to the fluid

varying with time, $B =$ typical body dimension, $C_d =$ drag coefficient.

In this experiment, considering the square root of body dimension is the exposure area, according to the wind angle and the equation is satisfied for a particular time only. Therefore, ignore the time variable. So, the above equation will be:

$$F_D = \frac{1}{2}\rho v^2 A C_d \qquad (11)$$

Here, A is the effective frontal area. The drag force on X and Y axes is calculated using CFD simulation, and other drag forces about the same axes calculated according to their effective frontal area with a constant wind density and velocity.

The wind force acting on the Models A, B, C, D in 0° and 90° wind angle which is parallel to the Y and X axis, respectively, of the building models as shown in Fig. 1. The drag force coefficients (C_{fx}) parallel to X axis in 90° wind angle for Models A, B, C and D are shown in Fig. 15a and lift force coefficients (C_{fy}) parallel to Y axis for 0° wind angle are shown in Fig. 15b. The C_{fx} is maximum (1.213) for Model A with respect to the other three models and minimum (1.016) for Model D as shown in Fig. 15a. These alterations are due to the change of effective frontal area, which is gradually decreasing from Models A to D for 90° wind angle due to the setback distance of models. Similarly, minimum C_{fy} (1.165) located under Model A and maximum

Fig. 13 Comparison of maximum and minimum C_{pe} in percentage of length for Models A, B, C and D **a** for Roof R1, **b** for Roof R2
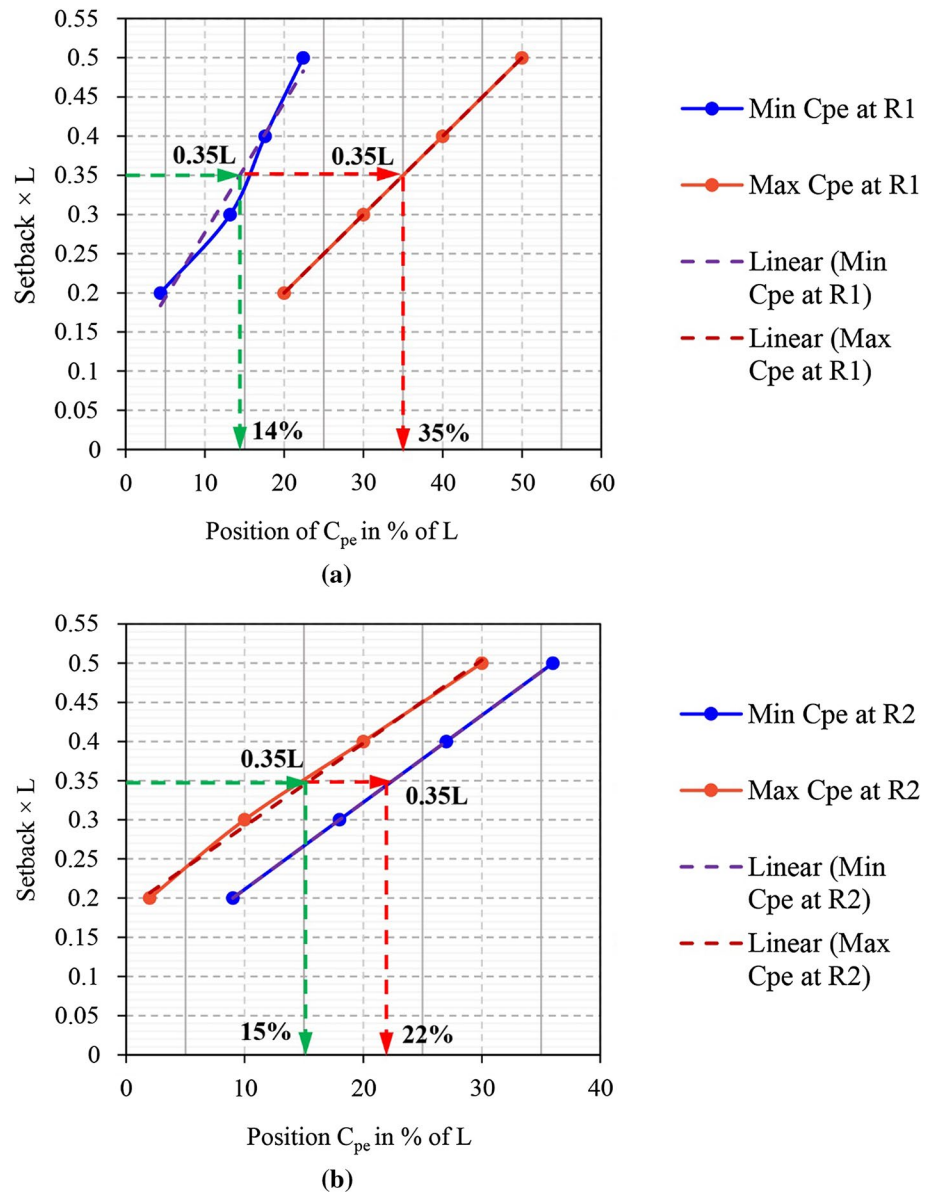

(1.252) under Model D as shown in Fig. 15b. This type of variation is due to the increase in velocity near the setback region, which is stated in the fluctuation of wind velocity section. Finally, it may be said that the drag on setback building depends upon the exposed area of the model and setback amount. When the exposed area and setback increase, the drag also increases.

3 Conclusion

The pressure and force coefficients are estimated after careful calculation using CFD simulation for different faces and the roofs of the building Models A, B, C and D with setback distance 0.2L, 0.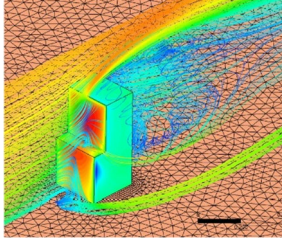3L, 0.4$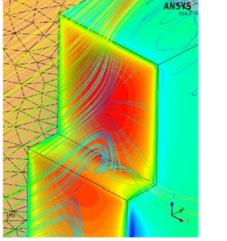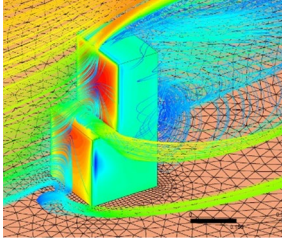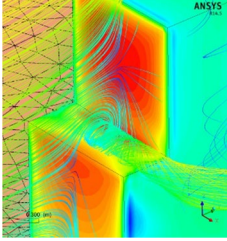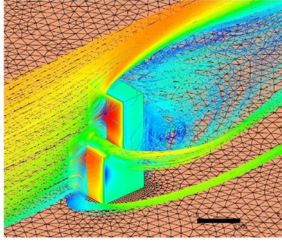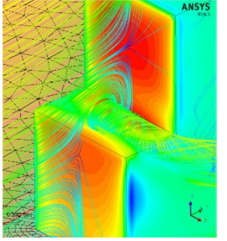L$ and 0.5L at H/2 level. A number of significant points are recorded during the analysis and this is concluded below.
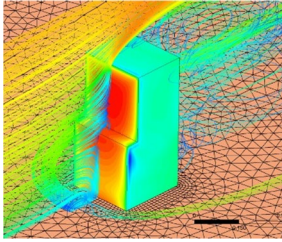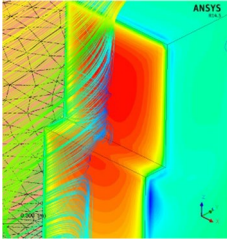
- Maximum positive pressure coefficients (C_{pe}) develop at 0.9H, i.e., 90% of the building height from the base of all the models at windward face for 90° wind angle.
- When the setback position is in the windward leadership, at that time maximum C_{pe} is located at 0.8H, which is 80% of the building height. This 80% height is consistent for any setback distance of windward face for 0° wind angle, if setback is placed at building mid height.
- High suction developed from 0.2 to 0.5L setback at the side face when wind angle is 0° at 12H/25 level due to the progressive increase in side wash by increasing the setback distance.

Table 9 Pressure contour of different faces and roofs for Models A, B, C and D for 0° wind angle
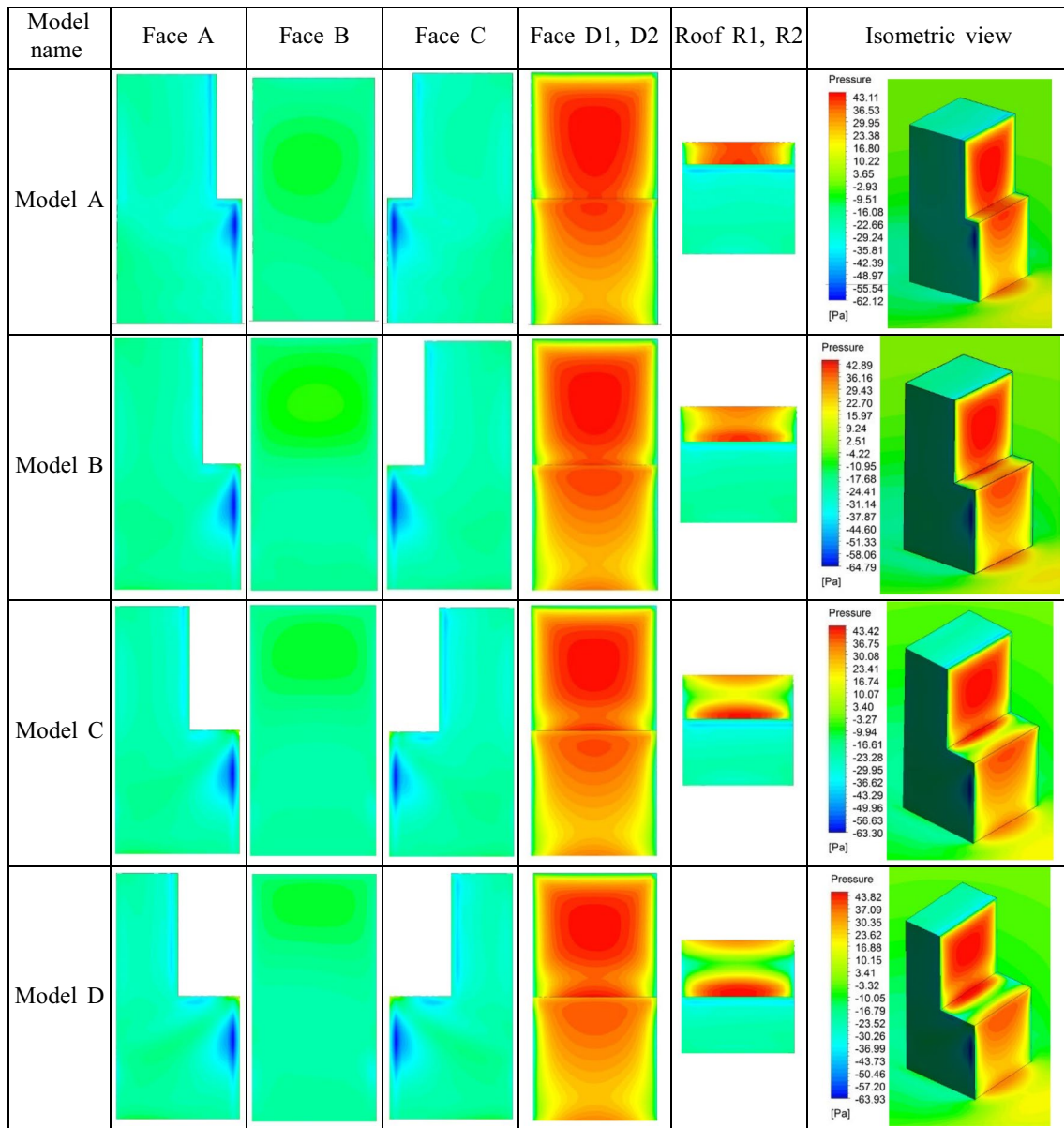
- Abrupt fall of positive pressure evolved at Face A, i.e., windward face for 90° wind angle, which is increasing from setback 0.2L to 0.5L at 12H/25 level. The fall of positive pressure in between 0.444 to 0.888L from 1′

point and the difference of pressure fall is a maximum 47.22% for setback 0.4L and minimum 23.75% for 0.3L.
- Pressure coefficient for 0° wind angle at Roof R1 is negative for all the models, at that moment C_{pe} is positive for

Table 10 Streamline for models A, B, C and D for 0° wind angle

Model name	Stream line	Close up view of stream line
Model A		
Model B		
Model C		
Model D		

Roof R2. Maximum and minimum positive pressures at R2 for all the models are situated in a linear way. In the meantime, the maximum C_{pe} at R1 constantly restored at the kink segment between Roof R1 and Face D2 for all the buildings. Therefore, special care should be considered while designing the setback roof.

- Local pressure evolved only at the lower sidewalls of all the building models. In this connection, low suction pressure develops due to the setback distance at the upper inset side walls; therefore no local pressure was generated at this belt for 0° wind.
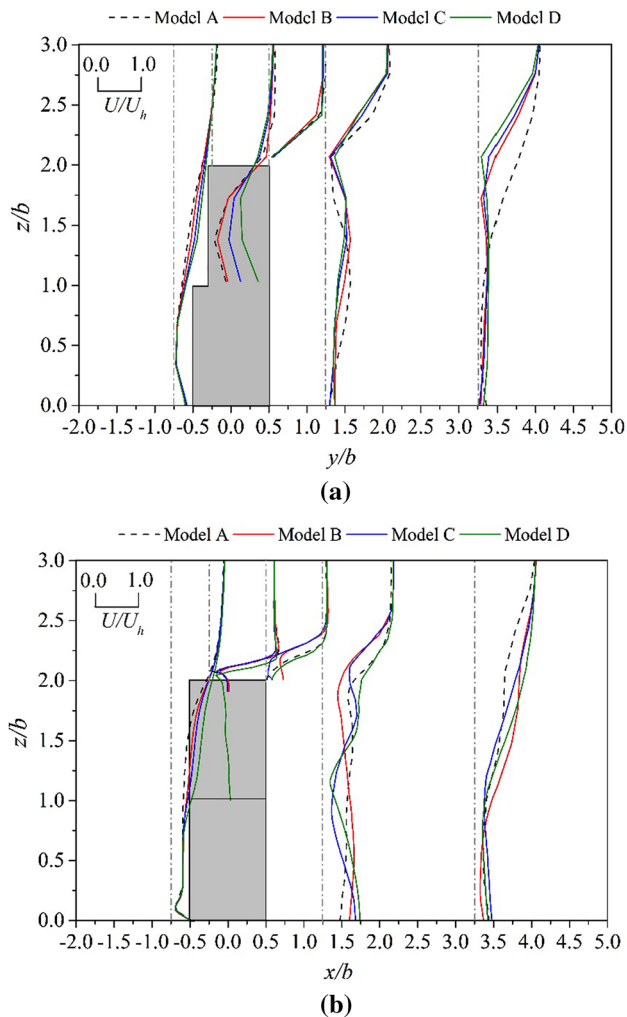
Fig.14 Non-dimensional streamwise velocity profile for Models A, B C and D at $-0.75, -0.25, 0.5, 1.25$ and 3.25 for **a** 0° wind angle ($x/b = 0$) and **b** 90° wind angle ($y/b = 0$)

Fig. 15 Force coefficient for Models A, B C and D **a** C_{fx} for 90° wind angle, **b** C_{fy} for 0° wind angle

setback distance is easily calculated for Models A, B, C and D.

- According to the non-dimensional velocity variation (U/U_h), it is said that the velocity is directly proportional to setback distance when setback is placed at the mid-height of the building.
- High amount of turbulence and velocity fluctuation is observed at the backside of the setback roof and top roof of the building model.
- The drag on setback building depends upon the exposed area of the model and setback amount. When the exposed area and setback increase, the drag also increases. Then it can be said that way, the drag is directly proportional to the exposed area of building surface and setback distance at mid-height of the building.
- According to the linear graph of maximum and minimum positive pressure at Roof R1 and R2, the C_{pe} in percentage of length of the building according to their respective
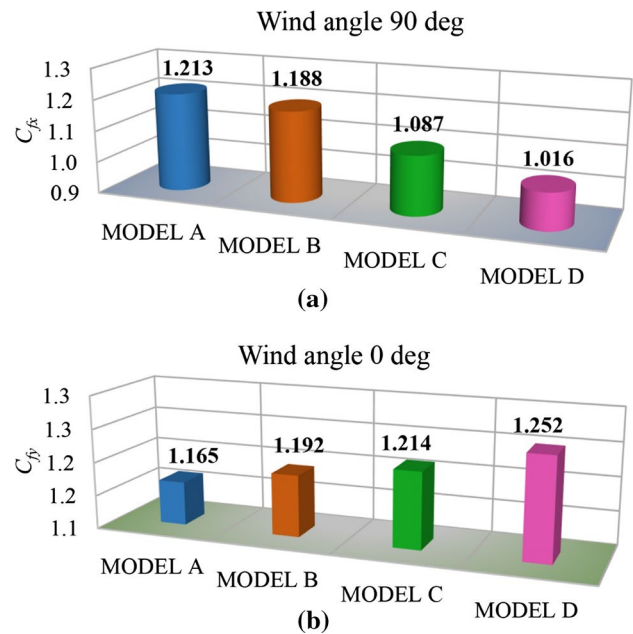
References

Amin JA, Ahuja AK (2010) Aerodynamic modifications to the shape of the buildings: a review of the state-of-the-art. Asian J Civ Eng (Build Hous) 11(4):433–450

ANSYS CFX-Solver Theory Guide (2012) Release 14.5, October

AS/NZS: 1170.2 (2002) Structural design actions, part 2: wind actions. Standards Australia/Standards New Zealand, Sydney, Wellington

ASCE/SEI: 7-10 (2010) Minimum design loads for buildings and other structures. Structural Engineering Institute of the American Society of Civil Engineering, Reston

Azzi Z, Habte F, Elawady A, Chowdhury AG, Moravej M (2020) Aerodynamic mitigation of wind uplift on low-rise building roof using large-scale testing. Front Built Environ 5(149):1–17

Baby S, Jithin PN, Thomas AM (2015) A study of wind pressure on tall buildings and its aerodynamic modifications against wind excitation. Int J Eng Dev Res 3(4):1–10

Bairagi AK, Dalui SK (2018) Comparison of aerodynamic coefficients of setback tall buildings due to wind load. Asian J Civ Eng Build Hous 19:205–221

Bairagi AK, Dalui SK (2019) Distribution of wind pressure around different shape tall building. In: 2nd International conference on emerging research in civil. Aeronautical and Mechanical Engineering, Bangalore

BS 6399-2 (1997) British standard: loading for buildings part 2. Code of practice for wind loads, British Standard Institution, London

Chan CM, Chui JKL, Huang MF (2009) Integrated aerodynamic load determination and stiffness design optimization of tall buildings. Struct Des Tall Spec Build 18:59–80

Elshaer A, Bitsuamlak G, Damatty AE (2016) Aerodynamic shape optimization of tall buildings using twisting and corner modifications. In: 8th International colloquium on bluff body aerodynamics and application. Northeastern University, Boston

EN 1991-1-4:2005/AC (2010) (E) European committee for standardization (CEN). Eurocode 1: actions on structures-part 1–4: general actions -wind actions. European Standard (Eurocode). European Committee for Standardization (CEN), Europe

Franke J, Hirsch C, Jensen A, Krüs H, Schatzmann M, Westbury P, Miles S, Wisse J, Wright NG (2004) Recommendations on the use of CFD in wind engineering. COST Action C14; impact of wind and storm on city life and built environment. Von Karman Institute for Fluid Dynamics

Franke J, Hellsten A, Schlünzen H, Carissimo B (2007) Best practice guideline for the CFD simulation of flows in the urban environment. COST Action 732

Gousseau P, Blocken B, van Heijst GJF (2013) Quality assessment of Large–Eddy simulation of wind flow around a high-rise building: validation and solution verification. Comput Fluids 79:120–133

Irwin P, Kilpatrick J, Robinson J, Frisque A (2008) Wind and tall buildings: negatives and positives. Struct Des Tall Spec Build 17:915–928

I.S: 875 (Part-3) (2015) Indian standard code of practice for the design loads (other than earthquake) for buildings and structures (part-3. wind loads). Bureau of Indian Standards, New Delhi

Jain A, Srinivasan M, Hart GC (2001) Performance based design extreme wind loads on a tall building. Struct Des Tall Spec Build 10:9–26

Kareem A (1992) Dynamic response of high-rise buildings to stochastic wind loads. J Wind Eng Ind Aerodyn 41(44):1101–1112

Kijewski-Correa T, Pirnia JD (2007) Dynamic behavior of tall buildings under wind: insights from full-scale monitoring. Struct Des Tall Spec Build 16:471–486

Kim Y, Kanda J (2010) Characteristics of aerodynamic forces and pressures on square plan buildings with height variations. J Wind Eng Ind Aerodyn 98:449–465

Kim YC, Kanda J (2013) Wind pressures on tapered and set-back tall buildings. J Fluids Struct 39:306–321

Kim YM, You KP, Ko NH (2008) Across-wind responses of an aeroelastic tapered tall building. J Wind Eng Ind Aerodyn 96:1307–1319

Kim YC, Kanda J, Tamura Y (2011) Wind-induced coupled motion of tall buildings with varying square planwith height. J Wind Eng Ind Aerodyn 99:638–650

Kwon DK, Kareem A (2013) Comparative study of major international wind codes and standards for wind effects on tall buildings. Eng Struct 51:23–35

Masera D, Ferro GA, Persico R, Sarkisian M, Beghini A, Macheda F, Froio M (2015) Effect of wind loads on non-regularly shaped high-rise buildings. In: 40th Conference on our world in concrete and structures. Singapore, pp 1–9

Mendis P, Ngo T, Haritos N, Hira A, Samali B, Cheung J (2007) Wind loading on tall buildings. Electron J Struct Eng Spec Issue Load Struct 7:41–54

Mendis P, Mohotti D, Ngo T (2014)Wind design of tall buildings, problems, mistakes and solutions. In: 1st International conference on infrastructure failures and consequences. Melbourne, Australia

Meng Y, Hibi K (1998) Turbulent measurements of the flow field around a high-rise building. J Wind Eng 76:55–64

Mittal H, Sharma A, Gairola A (2018) Numerical simulation of pedestrian level wind conditions: effect of building shape and orientation. Environmen Fluid Mech 20:663–688

Rej A, Bairagi AK (2019) Wind load analysis of a tall structure with sharp and corner cut edges. In: 2nd International conference on emerging research in civil. Aeronautical and Mechanical Engineering, Bangalore

Revuz J, Hargreaves DM, Owen JS (2012) On the domain size for the steady-state CFD modelling of a tall building. Wind Struct 15(4):313–329

Roy K, Bairagi AK (2016) Wind pressure and velocity around stepped unsymmetrical plan shape tall building using CFD simulation—a case study. Asian J Civ Eng BHRC 17(8):1055–1075

Shiva AAK, Gupta PK (2013) Wind loads on tall buildings with steps. J Acad Ind Res 1(12):766–768

Simiu E, Scanlan RH (1996) Wind effects on structures fundamentals and applications to design, 3rd edn. Wiley, New York

S.P 64 (S&T) (2001) Explanatory hand book on Indian standard code of practice for design loads (other than earthquake) for buildings and structures, part 3 wind loads [IS 875 (part 3): 1987]. Bureau of Indian Standards, New Delhi, India

Tanaka H, Tamura Y, Ohtake K, Nakai M, Kim YC, Bandi EK (2013) Aerodynamic and flow characteristics of tall buildings with various unconventional configurations. Int J High Rise Build 2(3):213–228

Tominaga Y, Mochida A, Murakami S, Sawaki S (2008a) Comparison of various revised k–ε models and LES applied to flow around a high-rise building model with 1:1:2 shape placed within the surface boundary layer. J Wind Eng Ind Aerodyn 96:389–411

Tominaga Y, Mochida A, Yoshie R, Kataoka H, Nozu T, Yoshikawa M, Shirasawaet T (2008b) AIJ guidelines for practical applications of CFD to pedestrian wind environment around buildings. J Wind Eng Ind Aerodyn 96:1749–1761

Wang D, Yu XJ, Zhou Y, Tse KT (2015) A combination method to generate fluctuating boundary conditions for large eddy simulation. Wind Struct 20:579–607

Weerasuriya AU, Jayasinghe MTR (2014) Wind loads on high-rise buildings by using five major international wind codes and standards. Eng J Inst Eng 3(47):13–25

Xie J (2014) Aerodynamic optimization of super-tall buildings and its effectiveness assessment. J Wind Eng Ind Aerodyn 130:88–98

Xu Z, Xie J (2015) Assessment of across-wind responses for aerodynamic optimization of tall buildings. Wind Struct Techno Press Ltd 21(5):505–521

Yan BW, Li QS (2015) Inflow turbulence generation methods with large eddy simulation for wind effects on tall buildings. Comput Fluids 116:158–175

Zils J, Viise J (2003) An introduction to high-rise design. Struct Mag pp.12–16

Zu G, Lam KM (2018) LES and wind tunnel test of flow around two tall. Build Staggered Arrange Comput 6(28):1–18